PHYSICAL REVIEW B **87**, 085302 (2013)

Schrödinger-Poisson calculations for scanning gate microscopy of quantum rings based on etched two-dimensional electron gas

T. Chwiej and B. Szafran

AGH University of Science and Technology, Faculty of Physics and Applied Computer Science, al. Mickiewicza 30, 30-059 Kraków, Poland

(Received 10 May 2012; revised manuscript received 4 January 2013; published 6 February 2013)

We present a systematic numerical simulation of the scanning gate microscopy experiment as performed on a quantum ring etched out of InGaAs/InAlAs heterostructure containing two-dimensional electron gas (2DEG). The present simulation accounts for 2DEG deformation under the presence of the tip, for modification of the electron charge trapped at the semiconductor/vacuum interface, for polarization effects at the interface, for the image charges related to the presence of the metal tip and for the three-dimensional character of the confinement. Once the potential is established by self-consistence of the Schrödinger-Poisson scheme, the linear conductance is evaluated by solution of the quantum scattering problem with several subbands at the Fermi level. We find that the conductance is a slowly varying function of the tip position in accordance with the experimental data. We study the high-pass-filtered conductance maps, which generally exhibit concentric patterns outside the ring area, and radial features inside the ring for negative charge at the tip. Influence of the surface charge and potential imperfections on conductance maps are also discussed.

DOI: 10.1103/PhysRevB.87.085302 PACS number(s): 73.63.Nm, 73.63.Kv

I. INTRODUCTION

In semiconductor heterostructures with two-dimensional electron gas (2DEG), the electron mean-free path and phase coherence lengths are comparable to the size of studied systems.[1] In these conditions, the linear conductance G is determined by the scattering properties of Fermi electron wave functions, which makes these systems an attractive playground for phase-coherent quantum transport studies. The potential landscape for the Fermi electrons results from a rather complex electrostatics and localization of charge carriers. Since relatively recently[2,3] local perturbation of this potential can be introduced intentionally by a charged probe of a floating gate. The technique known as scanning gate conductance microscopy[2,3] allows for tracing the electron trajectories in unconfined systems visualizing the magnetic focusing,[4,5] interference due to the elastic scattering,[6] semiclassical scarred orbits of quantum billiards,[7,8] charged islands in the quantum Hall effect regime,[9] branching of the electron flow,[10–12] the flow dynamics in quantum point contacts,[13–15] and Aharonov-Bohm interference in quantum rings.[3,16–19]

The present paper is inspired by scanning gate conductance mapping experiments[3,16–19] on etched InGaAs/InAlAs quantum rings. The raw experimental G maps[3,16–19] of the rings are dominated by slowly varying background in contrast to the experiments on less strongly confined systems.[4,5,10–15] In general, the details of scattered wave function[10–12] can be resolved from the experimental G maps only provided that the effective width of the potential perturbation introduced to 2DEG by the electron gas is small as compared to the Fermi wavelength λ_F. The InGaAs/InAlAs quantum rings[3,16–19] have a high 2DEG density of the order of 10^{12} cm^{-2} and the Fermi wavelength (λ_F) of the order of 20 nm, which is smaller than the width of the effective potential of the tip. The range of the effective tip potential can be deduced from measurements on closed Coulomb blockaded quantum dots.[20–23] An experiment[23] on quantum dots tailored from 2DEG indicated that the tip potential is close to a Lorentzian of width 280 nm for the tip floating about 230 nm above the gas. Calculations of Ref. 24 indicated that the Lorentzian form of the effective potential is also found for etched channels—for the tip above the axis of the channel—and that the potential width is independent of the electron density and close to the tip-gas distance. In the experiments on quantum rings,[3,16–19] this distance corresponds to 50 nm,[18] which largely exceeds λ_F. Nevertheless, the experimental G maps[3,16–19] exhibit universal features upon high-pass filtering with the radial fringes within the ring and concentric ones outside. The latter result from the electrostatic Aharonov-Bohm (AB) effect and evolve in the external magnetic field due to contribution from the magnetic AB phase shift.[16] The radial features can be attributed to the elastic scattering within the ring.[24]

The actual form of the tip potential is of a crucial importance for interpretation of experimentally accessed conductance maps. Usually the tip potential is taken in a form of closed formulas of Lorentzian,[17,19] Gaussian,[7,17,18] or generalized Coulomb[5,21] profiles. The latter well approximates the solution of the Poisson equation for free-standing nanowires placed between the tip and the conducting backgate.[21] The original potential of the tip charge as seen by 2DEG is of the Coulomb form. The charges present within the sample react to this potential and screen it leaving only a short range component. For unconfined 2DEG, the screening response of the sample follows the tip as it scans the surface, so the form of the effective potential is preserved when the tip floats above the structure. This is not necessarily the case for samples containing the lateral confinement.[7,8,10–12,22,23] For etched rings[3,16–19] when G signal is gathered from outside of the channels, the screening starts only at the edge of the sample, so a closed form of the tip potential independent of the tip position is evidently excluded. There is probably no alternative solution of the Schrödinger-Poisson problem to determine the actual current flow conditions. The first step was made in Ref. 24, where the conductance was determined based on a DFT solution for a strictly two-dimensional electron sheet with the tip assumed in a form of a fixed point charge. The present calculation includes possibly all the details of the sample that are of an importance for the effective potential of the tip: (1) the presence of the surface charge, which is—as we show below—an effective source of screening, (2) polarization effects at the semiconductor/vacuum/metal interface, and (3) a constant voltage (and not constant charge) applied to the tip. Moreover, as a progress with respect to Ref. 24, (4) the actual three-dimensional confinement of the electron gas is accounted for, (5) the experimental range of the surface charge density is reached, and (6) the effects of perturbed symmetry of the device are described. All these steps taken, the modeling becomes relatively close to the experimental conditions and the results can be compared to the experimental ones at the quantitative level. For that purpose, we proceed to high-pass filtering[16,18] (7) of the conductance maps reaching a close correspondence to the experimental data.

II. THEORY

A. Model structure and electrostatics

The model structure contained within the computational box is depicted in Fig. 1 (see the caption for the structure details). The current flows within the $\mathrm{In}_{0.7}\mathrm{Ga}_{0.3}\mathrm{As}$ quantum well sandwiched between $\mathrm{In}_{0.52}\mathrm{Al}_{0.48}\mathrm{As}$ barriers. The upper InAlAs barrier is δ-doped with donors. The conduction band offset between the $\mathrm{In}_{0.7}\mathrm{Ga}_{0.3}\mathrm{As}$ quantum well and $\mathrm{In}_{0.52}\mathrm{Al}_{0.48}\mathrm{As}$ barrier materials is as large as $\Delta E_c = 680$ meV,[25] hence all the donors of the barrier are ionized. For the dopant density $\rho_d = 2 \times 10^{12}$ cm^{-2}, the ionized donors release about 7000 electrons to the structure contained within the computational box. The freed electrons go to two locations: (1) the InGaAs quantum well forming the 2DEG and (ii) the semiconductor/vacuum interface where they localize at the surface. The tip of the probe is assumed in a form of a sphere of radius R_{tip} that floats at a distance h above the upper edge of the quantum well.

The tip influences the charge and potential distribution of the sample near the semiconductor/vacuum interface and deeper inside the 2DEG area. The dielectric constant mismatch at the semiconductor surface and the surface charge are crucial for realistic modeling of the structure. Nevertheless, for the evaluation of the conductance, we are in fact interested in the potential distribution within the semiconductor. In order to determine this distribution, account is taken for the presence of vacuum and the metal tip and we proceed using a standard approach:[26] we treat the entire space as filled by a semiconductor and the effects of the dielectric constant discontinuities in the semiconductor/vacuum/metal interfaces are described using the image charge technique. The dielectric constant discontinuity between InAlAs/InGaAs is small and we neglect it.

In the experiment, the channels and the ring are formed by etching a layer structure. In this paper, we assume that the etched area is filled with a material that is dielectrically matched to InGaAs and does not contain any charge densities. This assumption allows us to use a simple form of the image charge technique for the planar surface between the dielectric and vacuum. We assume that the filling material has the bottom of the conduction band aligned with the InAlAs barrier to describe the electron confinement within the channels.

The surface of the structure is charged with electrons. The properties of the surface states at a clean InGaAs/vacuum interface are relatively well known.[27–29] We use the empirical parametrization[27–29] of the surface charge density to account for the screening of the tip by the surface charge, which occurs when the electron states are filled or emptied in reaction to the potential of the tip. Moreover, the electron charge is also accumulated at etched lateral trenches, which leads to a significant depletion of the 2DEG at the edges.[18] Here, we account for this effect according to the previous modeling[16–18] by reduction of the width of the channels with respect to the nominal (lithographic) geometry of the sample.

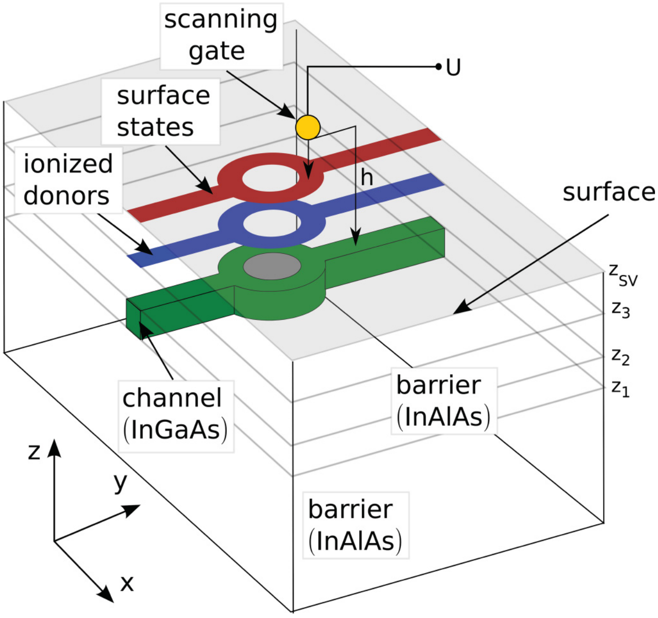

FIG. 1. (Color online) Schematics of the structure. The colored layers show the spatial distribution of charges included in the simulation. The computational box starts at $z = 0$ at the interface of heavily n-doped InP substrate and a thick layer of $\mathrm{In}_{0.52}\mathrm{Al}_{0.48}\mathrm{As}$ (barrier material). The latter corresponds to the lowest layer within the box [$z \in (0,z_1 = 110$ nm)] and is followed by a 13-nm-wide $\mathrm{In}_{0.7}\mathrm{Ga}_{0.3}\mathrm{As}$ quantum well [$z \in (z_1,z_2 = 123$ nm)]. On the quantum well layer, there is a 25-nm-thick barrier [$z \in (z_2,z_{\mathrm{sv}} = 148$ nm)] that tops the semiconductor structure. Inside this layer, 11 nm above the upper edge of the quantum well ($z_3 = 134$ nm), there is a monolayer δ-doped with Si donors of concentration $\rho_d = 2 \times 10^{12}$ cm^{-2}. The surface charge is confined at the semiconductor/vacuum interface. The structure is etched leaving a 120-nm-wide channel and a ring of inner radius of $r_{\mathrm{in}} = 140$ nm and the outer one with $r_{\mathrm{out}} = 280$ nm. In the model, the etched area is filled by the barrier material and deprived of any charges. The length of the channels inside the computational box is 700 nm. The computational box covers also the vacuum area up to 255 nm above the semiconductor structure. The scanning tip is assumed in a form of a sphere of a radius R_{tip} placed at a distance h above the upper edge of the quantum well.

The density of states localized at the lateral etched edges of the sample is unknown. We demonstrate below, that application of density states of (001) InAlAs/vacuum surface to the lateral edges drastically reduces the amplitude of the signal gathered when the tip is not right over the quantum ring, which is in an evident contradiction with the experimental data. Our calculation suggests, therefore, that the charge at the edged trenches is rigid and not very sensitive to the potential of the tip, and does not participate very effectively in the screening of

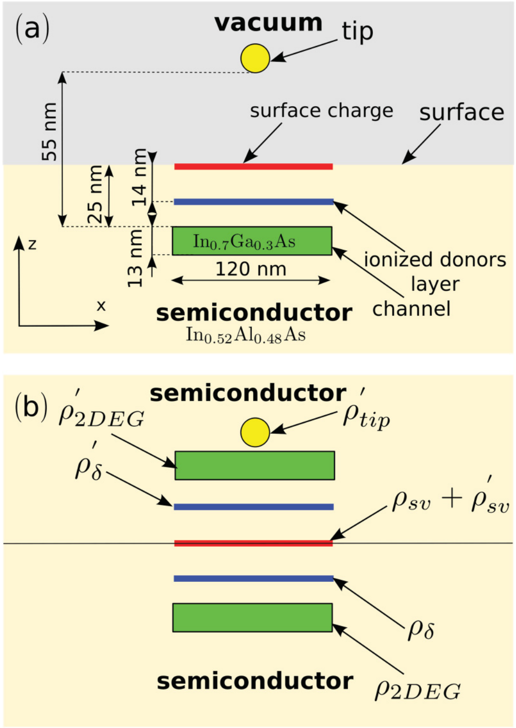

FIG. 2. (Color online) (a) Layers of the real charge present within the system. The surface charge is assumed at the semiconductor side of the solid/vacuum interface. (b) Model system applied for solution of the electrostatics within the semiconductor, extending the solid area to the entire space and including the image charges of the electron gas ρ'_{2DEG}, the dopant layer ρ'_{δ}, and the surface charge ρ'_{sv}.

the tip. Therefore the plain reduction of the area accessible to 2DEG near the edges due to the electrostatic repulsion by this charge seems quite a reasonable idea. According to Ref. 18 the lithographic width of the rings is up to nearly 200 nm, and the lateral gas depletion width is 35 nm. We study here mostly systems with channel widths of 120 (input and output channels) to 140 nm (ring channel).

The electrostatic potential on the semiconductor side is calculated from the Poisson equation

$$\nabla^2 V = -\frac{4\pi}{\epsilon_0\epsilon}\rho_{\text{tot}}, \tag{1}$$

where $\epsilon = 12.4$ is the applied semiconductor dielectric constant and ρ_{tot} stands for all the real and image charges present within the semiconductor structure and in the vacuum region. The real charges include [see Fig. 2(a)] the electron gas within the channel, the ionized dopants, the surface charge, and the charge localized at the tip. The treatment of the surface and image charges [see Fig. 2(b)] is explained in detail below. The Poisson equation is solved with a finite difference technique with the mesh spacings of $\Delta x = \Delta y = 3$ nm and $\Delta z = 1$ nm, using a fast Fourier transform technique.

1. *Surface charge*

The experimental structure is based on materials lattice matched to InP substrate that have been under intensive studies for the last two decades. In particular, the experimental analysis[27] of the $In_{0.52}Al_{0.48}As$ surface states indicated that they are distributed within two separate regions within the energy gap. The density of the surface states was parameterized in Refs. 28 and 29 and we use this parameterization in the present work. The surface electron density is evaluated as

$$\rho_{\text{sv}} = N_0 \sum_{i=1}^{2} n_i r_i F_i, \tag{2}$$

where N_0 is the surface atom density, n_i is the electric charge on a single surface state, r_i is the geometry factor, and F_i is the filling of the given surface state by the electrons given by

$$F_i = \int_{-E_g+V_s}^{V_s} dE \, \frac{\exp\left(-\frac{\{E-[V_s(\mathbf{r})-V_s^i]\}^2}{2\sigma_i^2}\right)}{\sqrt{2\pi}\sigma_i} \frac{1}{\exp\left(\frac{E-E_F}{kT}\right)}, \tag{3}$$

where the last term in the integrand is the Fermi-Dirac distribution ($T = 4.2$ K), V_s^i is the center of the ith surface state, and σ_i is its dispersion. The integration goes over the energy gap of the InAlAs barrier material. The energy shift $V_s(\mathbf{r}) = \Delta E_c - eV(\mathbf{r}) + S$ accounts for the conduction band offset between the InGaAs and InAlAs and the electrostatic potential energy at the given position at the surface. The value of S is a potential shift that gives the position of InGaAs conduction band with respect to the Fermi energy of the leads, determined by the charge neutrality condition (see below).

For most of the calculations, we adopted model parameters for the surface states density of Ref. 28, with $n_1 = n_2 = 1$, $N_0 = 5.8 \times 10^{14}$ cm^{-2}, $V_s^1 = 1000$ meV, $\sigma_1 = 80$ meV, $r_1 = 0.002$, $V_s^2 = 690$ meV, $\sigma_2 = 30$ meV, and $r_2 = 0.001$. We refer to this sets of values as parameterization I, and we use it throughout the paper unless explicitly stated otherwise. For the sake of discussion we also performed calculations with another set of parameters adopted of Ref. 29. According to parameterization II,[29] we use, $r_1 = 0.000794$, $r_2 = 0.000605$, $V_s^1 = 1000$ meV, and $V_s^2 = 620$ meV (other values as in I).

Figure 3 shows the surface states densities obtained with the parameterization I (black line, grey area) and II (red lines, red area). According to the second parameterization, the

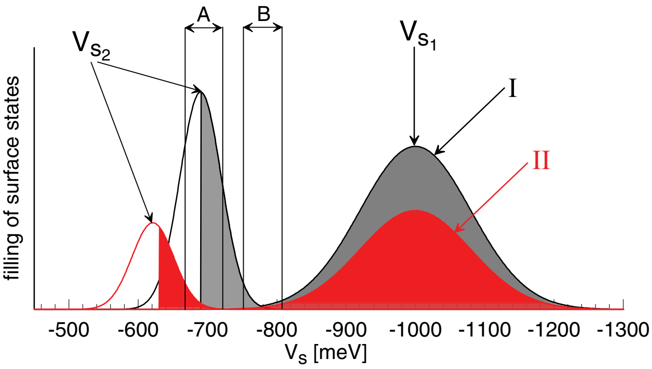

FIG. 3. (Color online) The surface states density with respect to $In_{0.52}Al_{0.48}As$ conduction band for applied parameterizations I (black line) and II (red line), see text. The filled areas correspond to the occupied electron states for the Fermi energy near the center of the higher surface state.

surface confines smaller electron charge. We find that for the first (second) parameterization, most of the electrons freed by the donor impurity go to the surface (2DEG).

The extent to which the surface charge density reacts to the tip varies strongly with the local potential energy. In particular, for parameterization I, the reaction of the surface charge and this screening is strongest in region "A" and weakest in region "B." For the studied structure, we find that in parameterization I, the electrostatic potential at the surface in the absence of the tip is established rather within the B area with fully filled first level. For the parameterization II, also the second level tends to be filled.

2. *Image charges and tip charge*

The studied structure contains media (semiconductor/vacuum/metal) of very different dielectric properties. The dielectric constant discontinuities are accounted for by introducing the images of charges present within the semiconductor (1) at the vacuum side and (2) on the metal tip [see Fig. 2(b)].

(1) The image of charges present within the semiconductor $\rho_s(x,y,z)$ appear at the vacuum side in point $(x,y,2z_{\text{sv}}-z)$, in the scaled form $\rho_s'(x,y,2z_{\text{sv}}-z)=\frac{\epsilon-1}{\epsilon+1}\rho_s(x,y,z)$. The surface charge ρ_{sv} is assumed totally on the semiconductor side but close to the surface, hence its image appears within the vacuum area.

(2) The charges from the semiconductor area $\rho_s(\mathbf{r})$ with $\mathbf{r}=(x,y,z)$ produce images in the metal tip which is assumed of a spherical shape. The image charge is[26] $\rho_1=-\frac{R_{\text{tip}}}{u}\frac{2}{\epsilon+1}\rho$, where $\mathbf{r}_t$ is the center of the tip and $\mathbf{u}=\mathbf{r}-\mathbf{r}_t$. This image charge is localized at $\mathbf{r}_1=\mathbf{r}_t+\mathbf{u}\frac{R_{\text{tip}}^2}{u^2}$.

The original charge accumulated at the tip—modeled as a metal sphere of a radius R_{tip}—is determined as $q_0=U_tR_{\text{tip}}$, where U_t is the potential applied to the tip. The actual charge accumulated on the surface produce the same potential outside the tip as the point charge localized in $\mathbf{r}_t$. For finite difference mesh, the point charge is equivalent to the charge distribution $\rho_0=\frac{q_0}{\Delta x\Delta y\Delta z}$ contained within a single mesh cell.

The charge of the tip, $\rho_{\text{tip}}^1=\rho_0+\rho_1$ (the original one plus the image of the semiconductor charges), generates an image in the semiconductor given by $\rho_1''=-\frac{\epsilon-1}{\epsilon+1}\rho_{\text{tip}}$. The position of this image is $\mathbf{r}_1''=(x_1,y_1,2z_{\text{sv}}-z_1)$. The image of the tip within the semiconductor generates on its turn the image within the spherical tip $\rho_2=-\rho_1''\frac{R_{\text{tip}}}{u''}$, where $\mathbf{u}''=\mathbf{r}_1''-\mathbf{r}_t$. The charge of the tip is therefore a sum[26] of three components $\rho_{\text{tip}}=\rho_0+\rho_1+\rho_2$. Calculation of ρ_1 and ρ_2 is done by a self-consistent iteration with convergence reached after about 20 iterative steps.

The entire charge density as seen from the semiconductor area including the image charges is given by $\rho_{\text{tot}}=\rho_s+\rho_s'+\frac{2\epsilon}{\epsilon+1}\rho_{\text{tip}}$ and this density appears in Poisson equation (1) to be solved.

3. *Boundary conditions*

The boundary conditions for the Poisson equation seen in the extended semiconductor area [see Fig. 2(b)] are calculated in the following manner. The computational box is assumed charge neutral. At the sides of the computational box [see Fig. 1] that are crossed by the leads we assume $\frac{\partial V}{\partial y}|_{y=\pm y_b}=0$, where $\pm y_b$ are the coordinates of two sides of the computational box. On the remaining four sides of the computational box the electrostatic potential is calculated from the charge density present within the computational box and introduced to the Poisson equation via Dirichlet type boundary condition. The values of the potential are calculated using the multipole expansion technique.[26] For that purpose, we extended the computational box by 700 nm of both sides including the leads. The extended region was filled with charge density of the edges of the original computational box. Then the extended computational box was divided into subdomains of size $l_x\times l_y\times l_z$ with $l_x=l_y=l_z=20$ mesh points. Within each subdomain the charge, the dipole and quadrupole moments were calculated. The results for the charge moments in each subdomain are next used for establishing the potential distribution on the sides of the box.

B. The electron gas

We solve the Schrödinger equation for the electrons localized within the InGaAs channels to establish the electron charge density, which enters the Poisson equation for the device, and to solve the scattering problem for the electron at the Fermi surface in order to evaluate the conductance. The single-electron Hamiltonian is of the form

$$\widehat{H}=\widehat{P}_{xy}+\widehat{T}_z+W(\mathbf{r}),\tag{4}$$

where $\widehat{P}_{xy}$ and $\widehat{T}_z$ are the kinetic energy operators within the (x,y) and z directions, respectively, and W is the confinement potential, with $W(x,y,z)=V(x,y,z)+V_{\text{xc}}(x,y,z)+V_{\text{well}}(z)+S$, where V is the electrostatic potential calculated from the Poisson equation (1), V_{xc} is the DFT exchange-correlation potential (we apply Perdew and Zunger parameterization[30]), $V_{\text{well}}=0$ inside the InGaAs quantum well and $V_{\text{well}}=\Delta E_c$ outside, and S is the constant energy shift mentioned above in the context of the surface states.

The kinetic energy component in the growth direction $\widehat{T}_z=-\frac{\hbar^2}{2}\frac{\partial}{\partial z}\frac{1}{m^*(z)}\frac{\partial}{\partial z}$ accounts for the discontinuity of the electron effective mass, which is significant with $m_0=0.04m_0$ for InGaAs the quantum well and $m_0=0.085m_0$ for InAlAs barrier. In order to account for the magnetic field $\mathbf{B}=(0,0,B)$, we apply the gauge $\mathbf{A}=(0,Bx,0)$, which gives

$$\widehat{P}_{xy}=\left[\widehat{p}_x^2+(\widehat{p}_y+eBx)^2\right]/2m^*.\tag{5}$$

Since the vertical confinement of the InGaAs channel (13 nm) is much stronger than the in-plane one (channel width of 120 nm), we apply an approximation of a frozen wave function within the z direction. For all the electrons, the three-dimensional wave function is then $\Psi_\mu(x,y,z)=\psi_\mu(x,y)f_0(z)$, where the same function f_0 is applied for all μ. With this assumption one can integrate out the z degree of freedom from the eigenproblem $\widehat{H}\Psi=E\Psi$. For that purpose, we multiply the eigenequation by $f_0(z)$ and integrate over z and obtain an effective two-dimensional problem:

$$[\widehat{P}_{xy}+\tilde{W}(x,y)-\tilde{E}]\psi(x,y)=0,\tag{6}$$

where $\tilde{W}(x,y)=\langle f_0(z)|W(x,y,z)|f_0(z)\rangle$, $\tilde{E}=E-T_z$, and $T_z=\langle f_0|\widehat{T}_z|f_0\rangle$. We do not make any further assumptions on

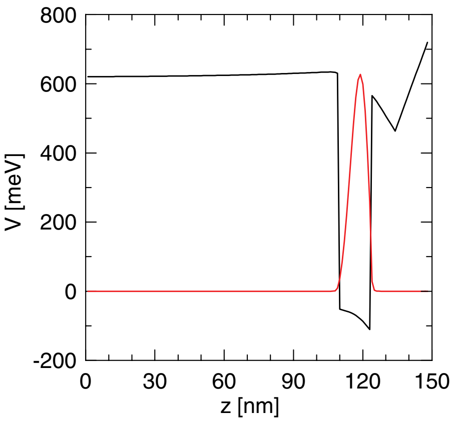

FIG. 4. (Color online) Potential $W(z)$ (black line) and the electron density $\rho_{2\mathrm{DEG}}$ (red line) in the asymptotic region along the line passing through the center of the channel ($x = 0, y = y_b, z$).

the specific form of $f_0(z)$, which is determined by a specific potential distribution within the self-consistent loop of the principal Schrödinger-Poisson calculation. For that purpose, we consider the potential along the z direction determined far away from the ring in the center of the lead, i.e., along the line $(0, y_b, z)$, see Fig. 4.

The eigenproblem (6) was solved in a basis of Gaussian functions with centers distributed on a mesh:[31]

$$\varphi_m(x,y) = \sum_{i=1}^{M_g} c_{m,i}\; g_i(x,y), \tag{7}$$

where

$$g_i(x,y) = \exp\left[-\frac{(x-x_i)^2+(y-y_i)^2}{2\sigma_g^2} - \frac{ieB}{\hbar}(y-y_i)x_i\right]. \tag{8}$$

Gaussians $g_i(x,y)$ are centers in nodes of a square mesh ($\mathbf{r}_i = [x_i, y_i]$), with the nearest-neighbor distance of $\Delta_g = \sqrt{2}\sigma_g$. For $\sigma_g = 6.56$ nm, the value of Δ_g is 9.28 nm.

In order to determine the expansion coefficients $c_{m,i}$ for Eq. (7), one solves the matrix eigenequation

$$\mathbf{H}\mathbf{c}_m = E_m \mathbf{P}, \tag{9}$$

in which $\mathbf{H}$ is the Hamiltonian matrix (6), with elements $h_{ij} = \langle g_i|\widehat{h}|g_j\rangle$, $\mathbf{P}$ is the overlap matrix of elements $p_{ij} = \langle g_i|g_j\rangle$, and $\mathbf{c_m}$ is the vector whose elements are the coefficients $c_{m,i}$ appearing in formula (7).

We evaluate the linear conductance G which defines the current at low bias: $I = GV_{\mathrm{bias}}$. The linear conductance is by definition independent of V_{bias} and is experimentally determined in the limit of residual bias (in Refs. 16–18 $\simeq 25\mu$V). In order to determine the charge density across the structure, we neglect this small difference between the voltages applied to the leads, which allows us to apply periodic boundary conditions for the wave functions $\Psi(x, y + 2y_b) = \Psi(x,y)$, where $2y_b$ is the length of the computational box. The periodic boundary conditions are applied by a modification of matrix elements $\mathbf{H}_{ij}$ and $\mathbf{P}_{ij}$ in a way to imply that the centers near the low-y end of the computational box are neighbors of those at the high-y end. This is done at the matrix element calculation stage by a virtual shift of the centers near the high (low) end of the channel by $\mathbf{R} = [0, -(Y_m + \Delta_g)]$ by ($\mathbf{R} = [0, (Y_m + \Delta_g)]$), where $Y_m = \max_{i,j=1,M_g} |y_i - y_j|$ is the maximal y-direction distance between the centers of the basis. This procedure is applied for those functions, which are localized at a distance equal or lower to $10\Delta_g$ from the ends of the computational box.

Upon solution of the single-electron eigenequation, one determines the density of the electron gas

$$\rho_{2\mathrm{DEG}}(\mathbf{r}) = -e\nu_s \sum_\mu |\Psi_\mu(\mathbf{r})|^2 \frac{1}{\exp\left(\frac{E_\mu - E_F}{kT}\right)}, \tag{10}$$

where the factor $\nu_s = 2$ accounts for the spin degeneracy (the Zeeman effect is neglected).

In 2DEG, the maximal electron kinetic energy determines the carrier density. We treat the Fermi energy as the reference energy level $E_F = 0$. For all the donors of the doped ionized layer, the Fermi energy is pinned by the electron reservoirs. The parameter S defining the potential W in Eq. (4) fixes the position of the bottom of the InGaAs quantum well with respect to the Fermi energy. For the calculation, we choose a value of S for which the entire computational box is charge neutral—for parameterization I, we obtain $S = -60.4$ meV and for parameterization II, $S = -110$ meV.

C. Conductance from transmission (Landauer approach)

Once the self-consistence of the Schrödinger and Poisson schemes as well as the charge neutrality are obtained, we proceed to the calculation of the scattering problem to determine the Fermi level electron transfer probability across the structure. For that purpose, we take the potential $\tilde{W}(x,y)$ as calculated within the channels far away from the ring, where it only depends on the x coordinate $\tilde{W}_1(x) = \tilde{W}(x, y \to \infty)$. For the adopted gauge, the single-electron wave functions in potential $\tilde{W}_1(x)$ have a separable form $\psi_{k_p,p}(x,y) = \phi^{\mathrm{in}}_{p,k_p}(x)e^{ik_p y}$, where $\phi^{\mathrm{in}}_{p,k_p}(x)$ is the pth subband wave function across the channel and k_p is the wave vector. Solutions of the Schrödinger equation for this form of wave functions in potential $\tilde{W}_1(x)$ give the dispersion relation, which is depicted in Fig. 5. For parameterization I as many as eight subbands are present at the Fermi level, and the values of the Fermi wave vectors k_p are determined by crossing of the subband with the Fermi energy $E_{p,k_p} = E_F = 0$ condition.

In order to calculate the linear conductance, we apply the Landauer-Büttiker formula,

$$G = -\frac{2e^2}{h} \sum_p \int_{E_F-\Delta E}^{E_F+\Delta E} dE\; T_p(E)\frac{df}{dE}, \tag{11}$$

which employs the transfer probability T_p for the electron incident from the subband p for the thermal spread of the Fermi level accounted in the integration limits of $\Delta E = 6kT$ for which $\int_{E_F-\Delta E}^{E_F+\Delta E}(-\frac{df}{dE})dE \simeq 0.995$. The procedure of evaluation of $T_p(E)$ is based on a 2D finite-difference real-space scheme employing the gauge invariant kinetic energy

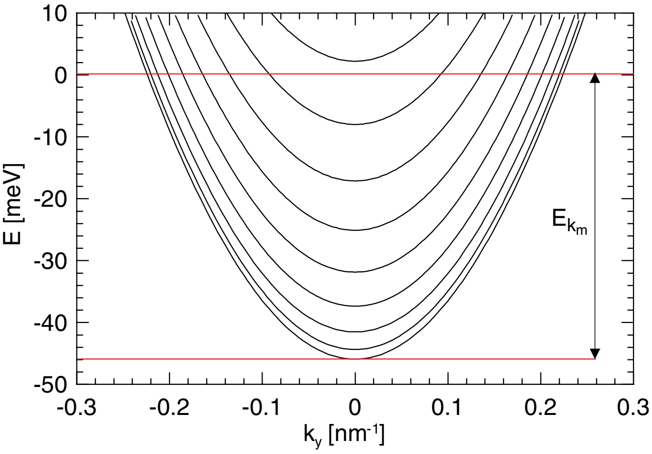

FIG. 5. (Color online) Dispersion relation for the electrons within the channel at $B = 0$. Eight subbands appear at the Fermi level, E_{k_m} is the kinetic energy of the Fermi electron motion along the wire in the lowest subband.

discretization[32] accounting for the multiband scattering and evanescent modes, which was described in detail in Ref. [24].

D. Calculation sequence

We first determine the equilibrium conditions for the electron flow solving the coupled Poisson and Schrödinger problems in the absence of the tip using the steps described above. The perturbation introduced by the tip to the potential and charge distribution within the 2DEG is weak—of the order of a few milli-electron-volts at maximum—compared to the kinetic energy of the progressive motion of Fermi electrons along the channels, which is of the order of 50–80 meV (depending on the parameterization of the surface states). For that reason, in order to determine the 2DEG charge density, we use the wave functions and the energy spectrum for the confined gas as calculated in the absence of the tip. The influence of the tip is introduced through the Fermi-Dirac distribution function,

$$\rho_{\mathrm{2DEG}}(\mathbf{r}) = -ev_s \sum_{\mu} |\Psi_\mu(\mathbf{r})|^2 \frac{1}{\exp\left[\frac{E_\mu - E_F + \Delta W(\mathbf{r})}{kT}\right]}, \qquad (12)$$

where the local perturbation introduced by the tip is $\Delta W(\mathbf{r}) = W_{\mathrm{tip}}(\mathbf{r}) - W_{\mathrm{notip}}(\mathbf{r})$, with W_{tip} and W_{notip} being the total potential energies in point $\mathbf{r}$ as calculated with and without the tip, respectively. In other words, the present scheme uses the solutions of the Schrödinger equation obtained in the absence of the tip for evaluation of the potential landscape for the Fermi level electrons that carry the current. The reaction of the electron gas to the tip is calculated as due to the variation of the local occupation of energy levels via the quantum statistics.

III. RESULTS AND DISCUSSION

A. Potential profile without the perturbation

For the parameterization I, the self-consistence is reached (without the tip) when 63% of the electrons provided by the donors go to the surface states and only 37% to the electron gas. Other properties of the 2DEG are listed in Table [I]. The average density of 2DEG inside the channel is then $n_{\mathrm{2DEG}} = 0.735 \times 10^{12}\ \mathrm{cm}^{-2}$ with eight subbands appearing at the Fermi level. For parameterization II, the surface adsorbs electrons less effectively. As much as 59.4% of the electron charge goes to 2DEG ($n_{\mathrm{2DEG}} = 1.19 \times 10^{12}\ \mathrm{cm}^{-2}$). In consequence, the kinetic energy of the highest occupied energy level grows to 76.1 meV, and as many as 11 subbands participate in the charge flow.

TABLE I. The kinetic energy of the lowest subband, its Fermi wavelength and wave vector for parameterization I. G stands for the calculated conductance of the ring.

B(T)	E_{k_m}(meV)	k_F(nm^{-1})	λ_F (nm)	$G(\frac{e^2}{h})$
0	45.91	0.224	28.1	5.36
0.5	45.55	0.248	25.4	5.02
0.515	45.52	0.2485	25.3	4.79

The self-consistent 2DEG charge and potential energy distribution W obtained in the absence of the tip for $B = 0$ T at 2 nm below the upper edge of the quantum well are displayed in Fig. [6]. The total potential [see Fig. [6(d)]] is rather flat inside the channels and takes minimal values at its edges. In consequence, the electron density [see Figs. [6(a)–6(c)]] is the largest at the edges of the structure. The electron density is rippled across the channels which is a result of the superposition of eight lowest subbands wave functions. The ripples are averaged out in the potential energy W. We note that on average the electron density is nearly equal within the ring and the channels.

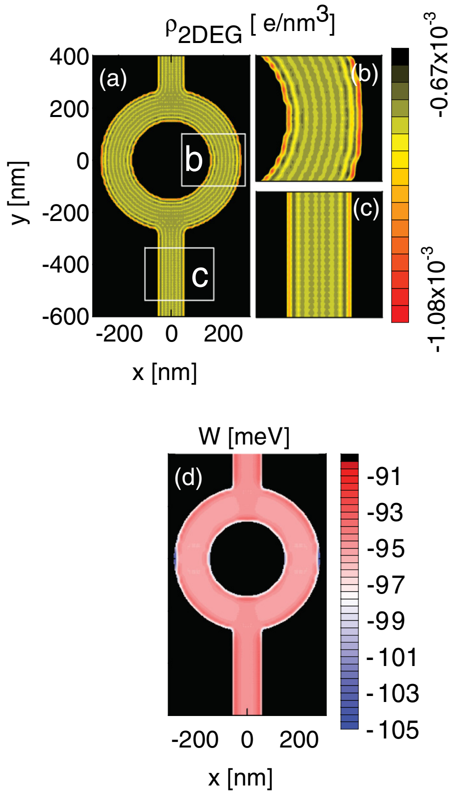

FIG. 6. (Color online) 2DEG charge distribution (a)–(c) and the total potential W at 2 nm below the upper edge of the quantum well.

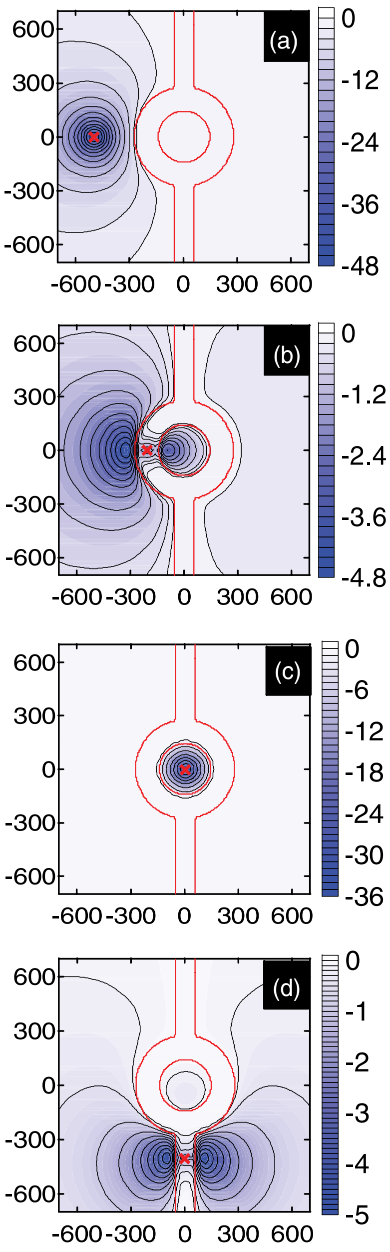

FIG. 7. (Color online) Potential distribution change $\Delta W = W_{\text{tip}} - W_{\text{notip}}$ (in milli-electron-volts) induced by the tip for $R_{\text{tip}} = 20$ nm and $U_t = 1$ V plotted 2 nm below the upper edge of the quantum well. The position of the tip is marked by the red dot.

Figure 7 shows the potential modification ΔW due to the tip ($R_{\text{tip}} = 20$ nm, $U_t = 1$ V, $h = 50$ nm, parameterization I) within the quantum well layer. For the tip outside the ring [see Figs. 7(a) and 7(c)], the potential change is limited to the edge of the channels. The potential within the channels is strongly affected only when the tip floats above them, see Figs. 7(b) and 7(d).

B. Radius of the tip versus *G* maps

Columns marked by G in Fig. 8 show the raw conductance maps for various radii of the tip R_{tip} and tip voltages U_t for $h = 50$ nm and $B = 0.5$ T. As a general rule, we notice that the raw conductance maps G are smooth functions of the tip position in agreement with the experimental data of Ref. 16. The columns denoted by δG in Fig. 8 show the high-pass Fourier filtered conductance—according to the technique used in postprocessing of the experimental data.[16,18] We calculate the Fourier transform of the conductance as a function of the tip position $G(x,y)$, obtaining its transform in the frequency domain $F[G(x,y)] = G(\omega_x,\omega_y)$. Then, $G(\omega_x,\omega_y) = G_1(\omega_x,\omega_y) + G_2(\omega_x,\omega_y)$, where G_1 covers the low frequencies $\sqrt{\omega_x^2 + \omega_y^2} < 4.2\ \text{nm}^{-1}$ and G_2 the rest of the higher frequencies. The columns marked in Fig. 8 as $\delta G(x,y)$ are calculated as the inverse Fourier transform of the high frequency part, i.e., $\delta G(x,y) = F^{-1}[G_2(\omega_x,\omega_y)]$.

In δG maps of Fig. 8, we notice that the ratio of the signal for the tip outside the channels to the signal for the tip inside the channels distinctly decreases with decreasing R_{tip}. An increased original charge ρ_0 is needed to maintain the same voltage for larger R_{tip}. For instance, at $U_t = -1$ V and for the tip localized above the axis of the channel far away from the ring, the total charge at the tip is $\rho_{\text{tot}} = -16.8e$ and $-41.7e$ for $R_{\text{tip}} = 20$ and 60 nm, respectively. For larger R_{tip}, the larger charge at the floating gate is placed at a larger distance from the electron gas. From the previous study,[24] we know that the effective width of the tip potential grows with the tip-electron gas distance, which explains the stronger signal from outside the ring for larger R_{tip}. In Fig. 8, we also notice that for larger R_{tip} the concentric fringes in the area outside the ring—a characteristic feature of the experimental data[16,18]—are well pronounced. In our data, radial features of δG inside the ring are usually observed for negative tip voltage, although occasionally they can be noticed also for positive voltage (see the result for $R_{\text{tip}} = 100$ nm and $U_t = +0.5$ V). As a general rule oscillations of the δG signal inside the ring are more abrupt for strong negative tip voltages. The presence of the repulsive potential of the tip enhances the electron backscattering.[24]

C. Screening induced by the surface charge

In order to demonstrate the role of the surface charge for screening and conductance maps, we performed calculations with the surface charge distribution established and fixed in the absence of the tip. The screening of the tip by the surface charge is in this way excluded. The results with frozen surface charge are plotted in Fig. 9 and should be compared to Fig. 8 with $R_{\text{tip}} = 20$ nm for $U_t = \pm 1$ V. As long as the background conductance G is concerned, no distinct change of the map is observed. However, the amplitude of δG variation when the surface charge is fixed increases more or less twice particularly for the tip above the channels.

Let us return to the results obtained with the surface charge reacting to the presence of the tip. The surface and 2DEG charge redistribution for the data of Fig. 8 for $R_{\text{tip}} = 20$ nm and $U_t = 1$ V is plotted in Fig. 10. Both the charges have the same sign, and react qualitatively similar to the presence of the tip. A positive potential of the tip is considered. We can see that the 2DEG charge is more distinctly increased along the edges of the channel. When the tip is above the channels the change of the surface charge density is about twice larger than the 2DEG charge density. This is related to the adopted

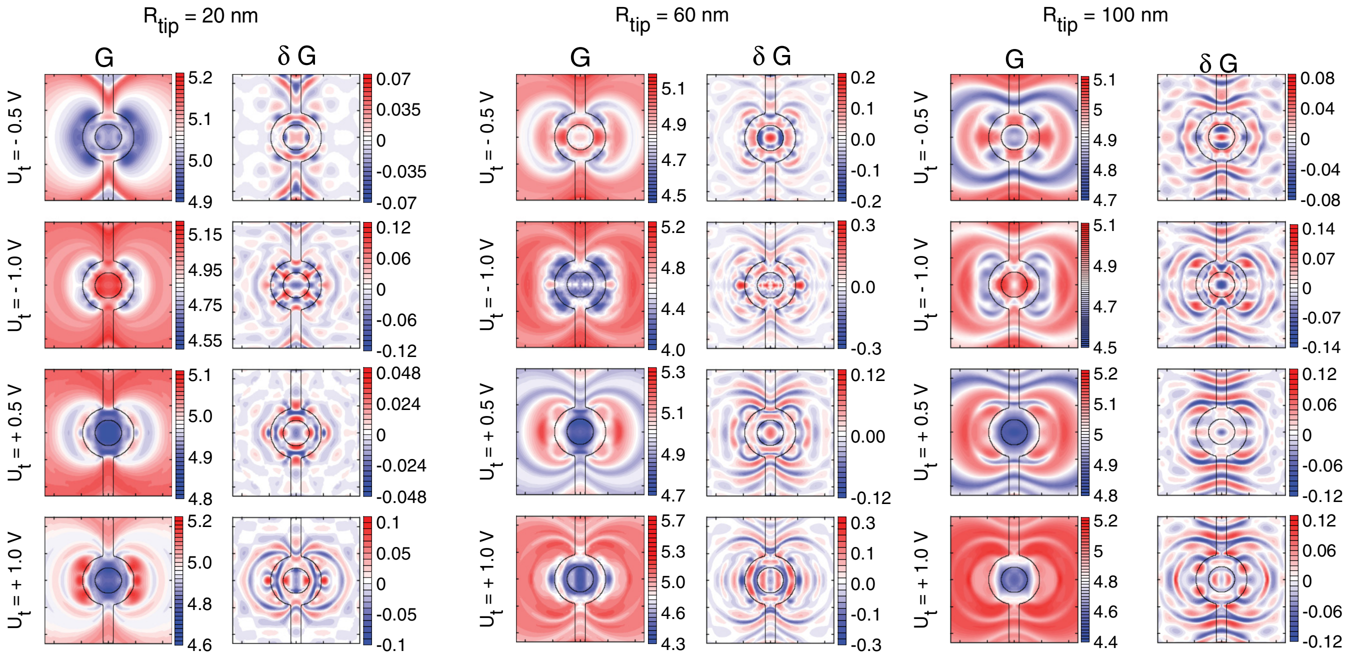

FIG. 8. (Color online) Raw conductance maps (G) and high-pass Fourier filtered signal δG for various radii of the tip R_{tip} for $h = 50$ nm and $B = 0.5$ T.

parameterization (I) of the density of surface states for which we find more electrons at the surface than in the 2DEG. Remarkably, when the tip is localized outside the channel in Fig. 10, we find that the maximal local change of the charge distribution is larger for 2DEG.

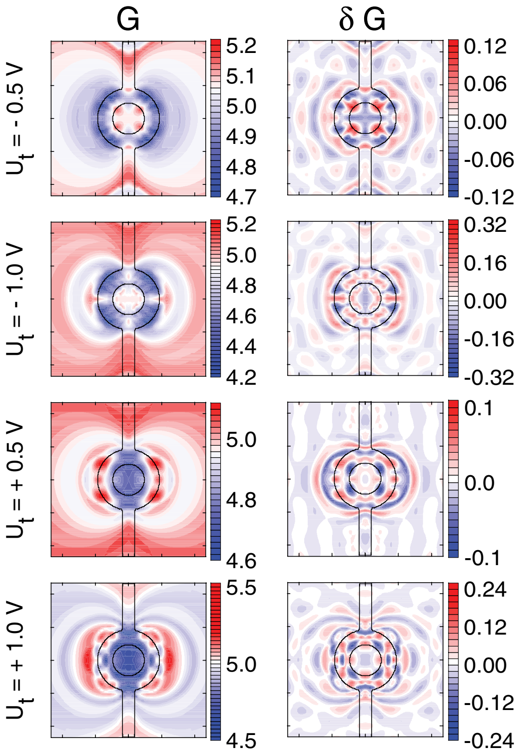

FIG. 9. (Color online) Same as Fig. 8 ($R_{\mathrm{tip}} = 20$ nm) only for switched off screening of the tip by the surface states (for the electron surface density fixed in the absence of the tip).

D. Charge at the lateral edges

In the bulk of this work, we neglect the charges accumulated at the lateral etched edges accounting for their presence by a limited width of the channels. In this section, we present the results which are obtained for the electrons adsorbed by the etched trenches. Due to lack of established density of states for the lateral surface, we used the parameterization I, which describes a clean (001) InAlAs/vacuum interface. We assumed that the lateral charge is localized up to the level of 50 nm below the surface of the structure. The electrostatic potential of the

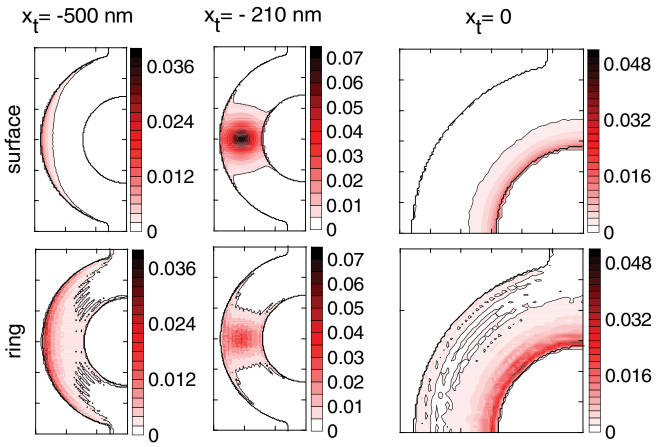

FIG. 10. (Color online) (Top) Surface electron density modification $\Delta\rho = \rho_{\mathrm{tip}} - \rho_{\mathrm{notip}}$ for $R_{\mathrm{tip}} = 20$ nm and $U_t = 1$ V. The maximal value of $\Delta\rho$ is 2×10^{14}, 7×10^{14}, and 2.5×10^{14} (in cm^{-2}), for the tip at $x_t = -500, -210$, and 0, respectively. (Bottom) Results for the 2DEG density 2 nm below the upper edge of the quantum well. The maximal value of $\Delta\rho$ is 3.8×10^{14}, 3.8×10^{14}, and 4.9×10^{14} (in cm^{-2}), respectively.

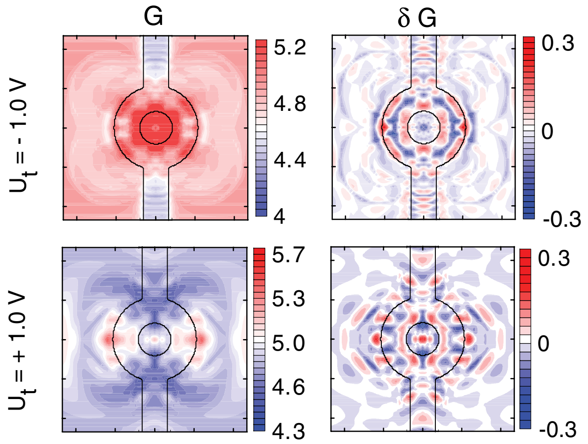

FIG. 11. (Color online) Same as Fig. 8 ($R_{\text{tip}} = 60$ nm) only with charge localized at the etched lateral edges of the structure with the density of states adapted from the surface of the system (parameterization I).

electrons at the lateral surface reduces the effective width of the channel and thus drastically increases the maximal kinetic energy of the electrons forming the Fermi gas. In order to keep the maximal kinetic energy unchanged with respect to the previous results, we increased the widths of the channels from 120 to 200 nm, with inner radii $r_{\text{in}} = 120$ nm and the outer one $r_{\text{out}} = 320$ nm. The results for $R_{\text{tip}} = 60$ nm are displayed in Fig. 11. As compared to the result of Fig. 8, we notice that the amplitude of the signal from outside the ring is drastically reduced. Moreover, the distinct concentric features of δG from outside the ring disappear. The present results in the context of the experimental data[16,18] suggest that the screening of the tip potential by the charges of the lateral trenches should not be very strong. This would be the case for large density of lateral surface states deep below the InGaAs conduction band, for which the lateral electron distribution will not significantly react to the tip potential.

E. Increased density of the electron gas

In this section, we applied the second parameterization of the surface states (see Sec. II A1) for which the electron density within 2DEG is nearly doubled. The results are given in Fig. 12. The data of Fig. 12(a), for $R_{\text{tip}} = 60$ nm, can be compared with the results of Fig. 8. We notice an increased amplitude of the signal and its stronger variation inside the ring.

Reference 18 reported on a presence of a region of linear dependence of the amplitude δG variation on U_t, for which the pattern of the map was essentially unchanged by U_t. In the present results, we notice a trend toward linearity understood in this way for increased (i) density of the 2DEG, (ii) tip-2DEG distance, and (iii) R_{tip}. An example is given in Fig. 12(b) for $R_{\text{tip}} = 100$ nm and $h = 70$ nm. Although the slowly varying background G changes strongly with U_t, the character of the δG map both inside and outside the ring retains much of its overall pattern, which was not the case in the data presented above.

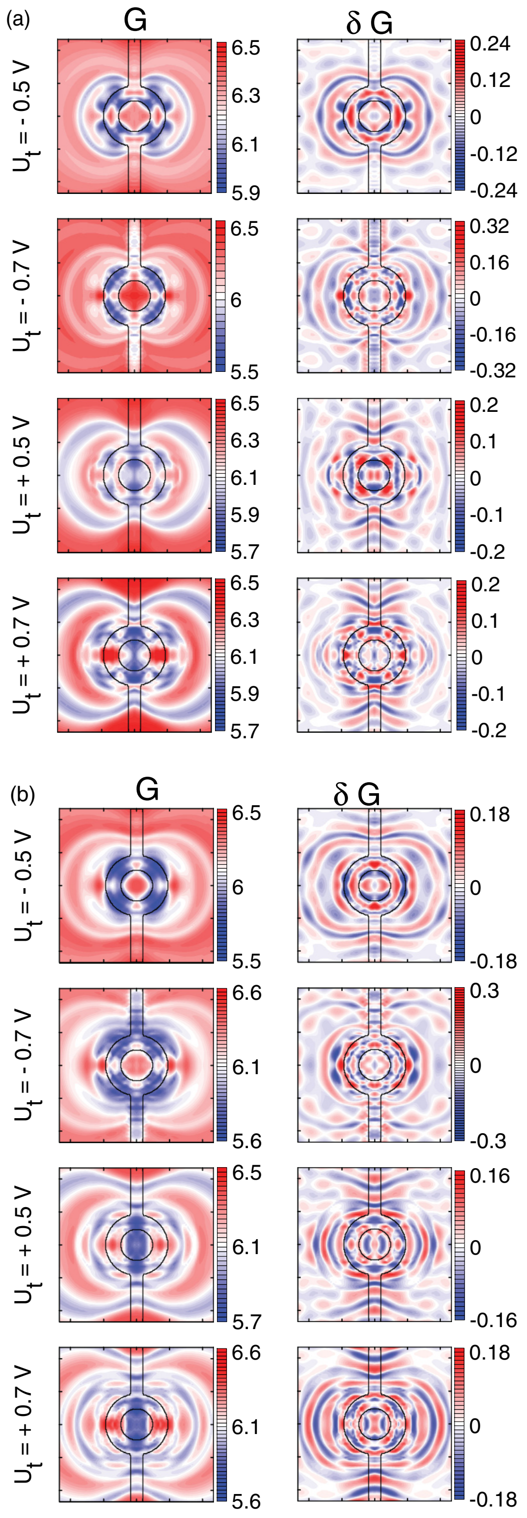

FIG. 12. (Color online) Same as in Fig. 8 only with parameterization II of the surface density with 59.4% electrons forming 2DEG, with (a) $h = 50$ nm, $R_{\text{tip}} = 60$ nm, and (b) $h = 70$ nm, $R_{\text{tip}} = 100$ nm.

F. Inhomogeneity of the ionized donor distribution

The results presented so far were obtained under an assumption that the structure has an ideal axial symmetry with respect to both $x = 0$ and $y = 0$ axes. The deviation of the actual structure from the perfect symmetry is inevitable.

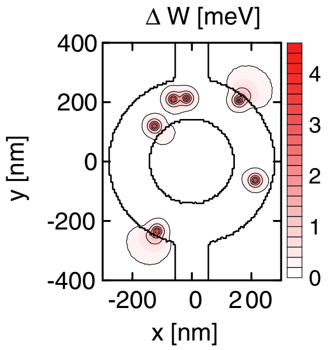

FIG. 13. (Color online) ΔW introduced by six negative charge centers 2 nm below the upper edge of the quantum well for $B = 0.5$ T.

In order to simulate the effects of the symmetry deviation, we performed calculations for inhomogeneity of the doping within xy plane. For 2×10^{12} impurities per cm^2, about 3000 donors are present above the ring area, and in the present model, we assume that their charge is uniformly smeared above the ring. Let us now assume that 0.2% of the dopants are missing, i.e., there are six donor impurities missing in the donor layer. The missing donors are accounted for by introduction of six negative charges localized at random within the doped layer. The potential perturbation introduced by the charges is depicted in Fig. 13, and the conductance map for this case is given in Fig. 14 for $R_{\rm tip} = 20$ nm at $B = 0.5$ [cf. the perfect ring results as given in Fig. 8]. Note that (1) the potential of the impurities is short range due to the screening by the rest of the charges and that (2) the actual positions of the charges are not visible in the conductance map of Fig. 14. Instead, all the plotted quantities are slightly deformed and rotated with respect to the unperturbed case. The overall character of the map for the perfectly symmetric potential is kept unchanged.

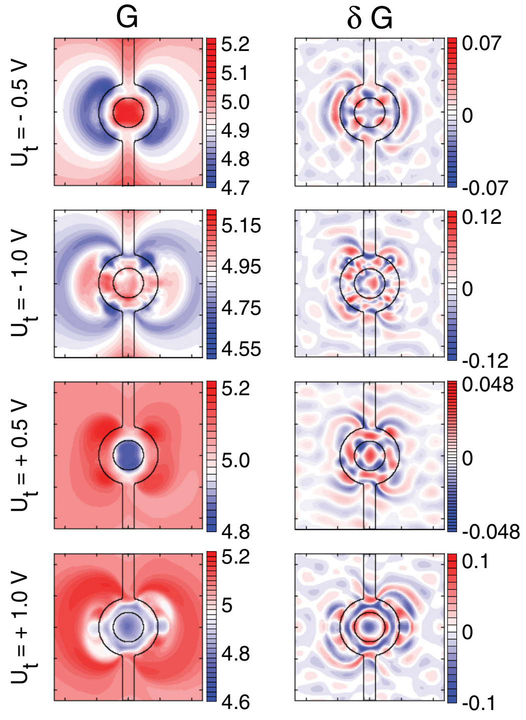

FIG. 14. (Color online) Same as Fig. 8 ($R_{\rm tip} = 20$ nm) only for unperfect doping simulated by six negative centers of Fig. 13.

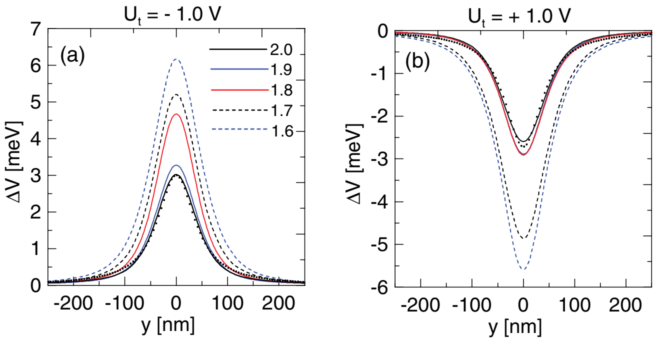

FIG. 15. (Color online) ΔW introduced by the tip as calculated along the axis of a straight channel for $R_{\rm tip} = 20$ nm. The numbers indicate the assumed density of donor centers [in 10^{12} cm^{-2} units] for $U_t = -1$ V (a) and $U_t = +1$ V (b). The dopant densities in units of 10^{12} cm^{-2} are given in the inset to (a).

G. Effective potential of the tip

For the purpose of conductance maps modeling, it would be useful to use a simple effective potential instead of the actual potential induced by the tip by massive numerical calculations. In order to inspect the form of the potential perturbation introduced by the tip, we calculated ΔW for a straight channel (without the ring) with the tip localized above the axis of the channel ($R_{\rm tip} = 20$ nm, $U_t = \pm 1$ V). The results are given in Fig. 15 for the quantum well layer. In Fig. 15, beside the nominal dopant concentration (2.0×10^{12} cm^{-2}), we considered also lower dopant concentrations. We see that the effective potential is close to a Lorentzian, $\Delta V = V_L/[1 + (r/\sigma_L)^2]$ whose width is largely independent on the dopant concentration. However, the maximal value of the Lorentzian increases quite fast with decreasing dopant concentration. For the donor concentration $\sigma = 2.0 \times 10^{12}$ cm^{-2}, the hight/width of the Lorentzian is $V_L = -2.71$ meV, $\sigma_L = 44.7$ nm for $U_t = 1$ V and $V_L = 3$ meV $\sigma_L = 44.17$ nm for $U_t = -1$ V. The width of the Lorentzian perturbation introduced thus exceeds the Fermi wavelength by a factor of 10 (see Table I).

We used the Lorentzian form of the effective potential to simulate the conductance maps calculated within the Poisson-Schrödinger scheme with the results presented in Fig. 16. We notice that the G maps obtained in this way for the tip outside the channels do not reproduce the features of the main simulation: the signal due to the tip vanishes quite fast. In the main simulation, the screening of the tip starts only at the edge of the channel, hence the signal has a long-range character due to the Coulomb interaction. The variation of δG and G inside the ring for the Lorentzian ansatz agree in amplitude with the results of the main simulation [see Fig. 8 for $R_{\rm tip} = 20$ nm and $U_t = \pm 1$ V]. Naturally, there is no correspondence between the results in the area outside the channels. Also, the relation of the G map inside the ring area as obtained by the ansatz

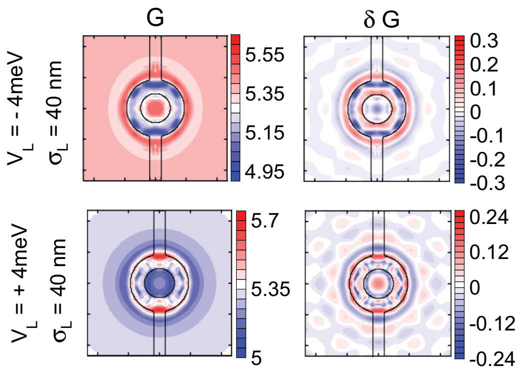

FIG. 16. (Color online) Same as Fig. 8 only for the potential of the tip replaced by a Lorentzian ansatz (see text).

potential to the ones obtained by the full procedure is rather unclear.

IV. SUMMARY AND CONCLUSIONS

In summary, we have solved the Schrödinger-Poisson problem for a model semiconductor structure simulating the conditions present in the experiments of conductance mapping by a floating gate. The present model accounts for the charge distribution within the two-dimensional electron gas, the spatial charge of the ionized donors, the surface charge and the dielectric constant discontinuities with metal, vacuum and semiconductor present within the computational box and the interactions between all the spatial charges. The solution of the self-consistent scheme produces the potential landscape for the Fermi electrons which determines the conditions for the electron transfer problem, which was solved by a direct approach to the Schrödinger equation with a full account taken for interband scattering. We discussed the charge (2DEG and surface charge) and potential distributions, and the conductance maps including its high-pass filtered part.

We have found that both the bare conductance and the high-pass filtered conductance exhibit rather circular features for the tip outside the ring, and the high-pass filtered part contains interlaced fringes of increased and decreased values in accordance with the experimentally stated tendency. The radial fringes, which are observed in the experiment, are found in the calculation when the tip is above the arms of the ring and when the tip charge is large and negative.

We have considered the potential disturbed by rigid charged point defects. The floating charges: the surface charge and the charge of the electron gas mask the presence of the point defects in the conductance maps, which keep their characteristic features with exception to some rotation and a deformation.

We have discussed the effective potential of the tip which turns out to be Lorentzian when the tip is above the axis of the channels. The Lorentzian width is independent of the electron gas density, which only influences the depth of the potential. The Lorentzian ansatz potential is not applicable when the tip is outside the ring and the channels. The Coulomb potential of the tip is screened only at their edges.

ACKNOWLEDGMENTS

This work was supported by National Science Centre according to decision DEC-2012/05/B/ST3/03290 and by PL-Grid Infrastructure. Calculations were performed in ACK–CYFRONET–AGH on the RackServer Zeus.

---

[1] S. Datta, *Electronic Transport in Mesoscopic Systems* (Cambridge University Press, Cambridge, 1995).

[2] D. K. Ferry, A. M. Burke, R. Akis, R. Brunner, T. E. Day, R. Meisels, F. Kuchar, J. P. Bird, and B. R. Bennett, Sem. Sci. Tech. **26**, 043001 (2011).

[3] H. Sellier, B. Hackens, M. G. Pala, F. Martins, S. Baltazar, X. Wallart, L. Desplanque, V. Bayot, and S. Huant, Sem. Sci. Tech. **26**, 064008 (2011).

[4] R. Crook, C. G. Smith, M. Y. Simmons, and D. A. Ritchie, Phys. Rev. B **62**, 5174 (2000).

[5] K. E. Aidala, R. E. Parott, T. Kramer, E. J. Heller, R. M. Westervelt, M. P. Hanson, and A. C. Gossard, Nat. Phys. **3**, 464 (2007).

[6] M. A. Topinka, B. J. LeRoy, S. E. J. Shaw, E. J. Heller, R. M. Westervelt, K. D. Maranowski, and A. C. Gossard, Science **289**, 2323 (2000).

[7] R. Crook, C. G. Smith, A. C. Graham, I. Farrer, H. E. Beere, and D. A. Ritchie, Phys. Rev. Lett. **91**, 246803 (2003).

[8] A. M. Burke, R. Akis, T. E. Day, G. Speyer, D. K. Ferry, and B. R. Bennett, Phys. Rev. Lett. **104**, 176801 (2010).

[9] B. Hackens, F. Martins, S. Faniel, C. A. Dutu, H. Sellier, S. Huant, M. Pala, L. Desplanque, X. Wallart, and V. Bayot, Nat. Commun. **1**, 39 (2010).

[10] M. A. Topinka, B. J. LeRoy, R. M. Westervelt, S. E. J. Shaw, R. Fleischmann, E. J. Heller, K. D. Maranowski, and A. C. Gossard, Nature (London) **410**, 183 (2001).

[11] M. P. Jura, M. A. Topinka, L. Urban, A. Yazdani, H. Shtrikman, L. N. Pfeiffer, K. W. West, and D. Goldhaber-Gordon, Nat. Phys. **3**, 841 (2007).

[12] M. G. Pala, S. Baltazar, P. Liu, H. Sellier, B. Hackens, F. Martins, V. Bayot, X. Wallart, L. Desplanque, and S. Huant, Phys. Rev. Lett. **108**, 076802 (2012).

[13] N. Aoki, C. R. Da, Cunham R. Akis, D. K. Ferry, and Y. Ochiai, Appl. Phys. Lett. **87**, 223501 (2005).

[14] A. Pioda, S. Kicin, D. Brunner, T. Ihn, M. Sigrist, K. Ensslin, M. Reinwald, and W. Wegscheider, Phys. Rev. B **75**, 045433 (2007).

[15] S. Schnez, C. Rössler, T. Ihn, K. Ensslin, C. Reichl, and W. Wegscheider, Phys. Rev. B **84**, 195322 (2011).

[16] B. Hackens, F. Martins, T. Ouisse, H. Sellier, S. Bollaert, X. Wallart, A. Cappy, J. Chevrier, V. Bayot, and S. Huant, Nat. Phys. **2**, 826 (2006).

[17] M. G. Pala, B. Hackens, F. Martins, H. Sellier, V. Bayot, S. Huant, and T. Ouisse, Phys. Rev. B **77**, 125310 (2008).

[18] F. Martins, B. Hackens, M. G. Pala, T. Ouisse, H. Sellier, X. Wallart, S. Bollaert, A. Cappy, J. Chevrier, V. Bayot, and S. Huant, Phys. Rev. Lett. **99**, 136807 (2007).

[19] M. G. Pala, S. Baltazar, F. Martins, B. Hackens, H. Sellier, T. Ouisse, V. Bayot, and S. Huant, Nanotechnology **20**, 264021 (2009).

[20] M. T. Woodside and P. L. McEuen, Science **296**, 1098 (2002); J. Qian, B. I. Halperin, and E. J. Heller, Phys. Rev. B **81**, 125323 (2010); E. E. Boyd, K. Storm, L. Samuelson, and R. M. Westervelt, Nanotechnology **22**, 185201 (2011).

[21] A. C. Bleszynski-Jayich, L. E. Fröberg, M. T. Björk, H. J. Trodahl, L. Samuelson, and R. M. Westervelt, Phys. Rev. B **77**, 245327 (2008); E. E. Boyd and R. M. Westervelt, *ibid.* **84**, 205308 (2011).

[22] M. Huefner, B. Kueng, S. Schnez, K. Ensslin, T. Ihn, M. Reinwald, and W. Wegscheider, Phys. Rev. B **83**, 235326 (2011).

[23] A. E. Gildemeister, T. Ihn, M. Sigrist, K. Ensslin, D. C. Driscoll, and A. C. Gossard, Phys. Rev. B **75**, 195338 (2007).

[24] B. Szafran, Phys. Rev. B **84**, 075336 (2011).

[25] B. Hackens, Ph.D. thesis Université Catholique de Louvain, 2005.

[26] J. D. Jackson, *Classical Electrodynamics* (John Wiley & Sons Inc., New York, 1962).

[27] W. Y. Chou, G. S. Chang, W. C. Hwang, and J. S. Hwang, J. Appl. Phys. **83**, 3690 (1998).

[28] G. S. Chang, W. C. Hwang, Y. C. Wang, Z. P. Yang, and J. S. Hwang, J. Appl. Phys. **86**, 1765 (1999).

[29] J. S. Hwang, G. S. Chang, W. C. Hwang, and W. J. Chen, J. Appl. Phys. **89**, 396 (2001).

[30] J. P. Perdew and A. Zunger, Phys. Rev. B **23**, 5048 (1981).

[31] T. Chwiej and B. Szafran, Phys. Rev. B **79**, 085305 (2009).

[32] M. Governale and C. Ungarelli, Phys. Rev. B **58**, 7816 (1998).